Photophysical behaviour of triethylmethylammonium tetrabromoferrate(III) under high pressure

Journal:	*Inorganic Chemistry*
Manuscript ID	ic-2023-02607a
Manuscript Type:	Article
Date Submitted by the Author:	28-Jul-2023
Complete List of Authors:	Nakagawa, Takeshi; Center for High Pressure Science and Technology Advanced Research, Ding, Yang; Center for High Pressure Science & Technology Advanced Research, X-ray Scattering group Bu, Kejun; Center for High Pressure Science and Technology Advanced Research, Lü, Xujie; Center for High Pressure Science and Technology Advanced Research, Liu, Haozhe; HPSTAR MOLITERNI, ANNA; Bari, Istituto di Cristallografia Popovic, Jasminka; Institut Ruder Boskovic, Division for Materials Physics Mihalik, Marian; Institute of Experimental Physics SAS, Magnetism Jaglicic, Zvonko; Instituta za matematiko fiziko in mehaniko, Dep. of Physics Mihalik, Matus; Institute of Experimental Physics SAS, Department of Magnetism Vrankić, Martina; Institut Ruder Boskovic,

SCHOLARONE™
Manuscripts

Photophysical behaviour of triethylmethylammonium tetrabromoferrate(III) under high pressure

Takeshi Nakagawa,[a] Yang Ding,[a] Kejun Bu,[a] Xujie Lü,[a] Haozhe Liu,[a] Anna Moliterni,[b] Jasminka Popović,[c] Marian Mihalik,[d] Zvonko Jagličić,[e,f] Matúš Mihalik,[d] Martina Vrankić*,[c]

[a]Takeshi Nakagawa, Center for High-Pressure Science & Technology Advanced Research, 100094 Beijing, P. R. China; takeshi.nakagawa@hpstar.ac.cn

[a]Yang Ding, Center for High-Pressure Science & Technology Advanced Research, 100094 Beijing, P. R. China; yang.ding@hpstar.ac.cn

[a]Kejun Bu, Center for High-Pressure Science & Technology Advanced Research,100094 Beijing, P. R. China; kejun.bu@hpstar.ac.cn

[a]Xujie Lü, Center for High-Pressure Science & Technology Advanced Research, 100094 Beijing, P. R. China; xujie.lu@hpstar.ac.cn

[a]Haozhe Liu, Center for High-Pressure Science & Technology Advanced Research, 100094 Beijing, P. R. China; haozhe.liu@hpstar.ac.cn

[b]Anna Moliterni, Institute of Crystallography (IC)-CNR, Via Amendola, 122/O, 70126, Bari, Italy; annagrazia.moliterni@ic.cnr.it

[c]Jasminka Popović, Division of Materials Physics, Ruđer Bošković Institute, Bijenička 54,10000 Zagreb, Croatia; jpopovic@irb.hr

[d]Marian, Mihalik, Institute of Experimental Physics, Watsonova 47, 040 01 Košice, Slovak Republic; mihalik@saske.sk

[e]Zvonko Jagličić, Institute of Mathematics, Physics and Mechanics, Jadranska 19, 1000 Ljubljana, Slovenia

[f]Zvonko Jagličić, Faculty of Civil and Geodetic Engineering, University of Ljubljana, Jamova 2, 1000, Slovenia; zvonko.jaglicic@imfm.si

[d]Matúš Mihalik, Institute of Experimental Physics, Watsonova 47, 040 01 Košice, Slovak Republic; matmihalik@saske.sk

[c]Martina Vrankić, Division of Materials Physics, Ruđer Bošković Institute, Bijenička 54, 10000 Zagreb, Croatia; mvrankic@irb.hr

Abstract. The pressure-induced properties of Hybrid Organic-Inorganic Ferroelectrics (HOIFs) with tunable structures and selectable organic and inorganic components are important for device fabrication. However, given the structural complexity of polycrystalline HOIFs and the limited resolution of pressure data, resolving the structure-property puzzle has so far been the exception rather than the rule. With this in mind, we present a collection of *in situ* high-pressure data measured for the triethylmethylammonium tetrabromoferrate(III), ($[N(C_2H_5)_3CH_3][FeBr_4]$) (**EMAFB**) by unraveling its flexible physical and photophysical behavior up to 80 GPa. Pressure-driven X-ray diffraction and Raman spectroscopy disclose its soft and reversible structural

distortion, creating room for delicate band gap modulation. During compression, orange turns dark red at ~2 GPa, and further compression results in piezochromism leading to opaque black, while decompressed **EMAFB** appears in an orange hue. Assuming that the mechanical softness of **EMAFB** is the basis for reversible piezochromic control, we present alternations in the electronic landscape leading to a 1.22 eV band narrowing at 20.3 GPa, while maintaining the semiconducting character at 72 GPa. The **EMAFB** exhibits an emission enhancement, manifested by an increase of photoluminescence up to 17.3 GPa, correlating with the onsets of structural distortion and amorphization. The stimuli-responsive behavior of **EMAFB**, exhibiting a stress-activated modification of the electronic structure, can enrich the physical library of HOIFs suitable for pressure-sensing technologies.

INTRODUCTION

Over the past couple of years, research on striking multifunctional application-aimed performances has sparked an unprecedented landscape of Hybrid Organic-Inorganic Ferroelectrics (HOIFs). In particular, it has opened up a fruitful field for exploring their superior structural diversity and versatile properties, highlighting the new directions in which the study and application of this group of materials are heading towards. Concomitantly, under the mantle of HOIFs, the multiferroic property and magnetoelectric effects form a backbone of information technology. The physical mechanisms behind the interplay of these materials' multiple physical effects have led to unprecedented advances in understanding their properties and have provided immense benefits to modern multifunctional devices and niche applications. Successful applications, especially in recent years, range from energy conversion devices,[1-3] sensors[4-6] and memory elements[7-10] to energy-efficient microelectronics[11]. To make materials smart for flexible

electronics, many efforts have been made to fabricate various ferroelectric and ferromagnetic heterostructures and novel topological oxides that exhibit these properties.[12-14] Similar to ferroelectric oxide materials, HOIFs have attracted much attention due to the increase in their structural degrees of freedom that result judiciously from the mediation of organic cations, providing diversified architectures and flexible frameworks that allow structural distortions that are otherwise forbidden in standard inorganic structures.[15] However, single-phase ferroelectrics containing hybrid inorganic-organic frameworks are rarer than inorganic oxides. Both multiferroicity and magnetodielectric coupling in metal-organic frameworks have so far been limited to formate-based systems with a perovskite structure, the largest subclass of multiferroic metal-organic frameworks, that are comprehensively described and discussed by Ma and Sun (2020)[16], Zheng *et al.* (2021)[17] and the most recent greatly addressed by Xiong *et al.* (2022)[18]. Screened out by their easily tunable bandgap and energy structure, high carrier mobility/absorption coefficient, and long carrier lifetime, some demonstrated excellent semiconducting properties comparable to, if not superior to, those of inorganic semiconducting ferroelectrics.[19-22] Despite these advances in recent years, indomitable effort searching for more HOIFs with desirable performance continues. From an applications standpoint, oxides typically have good chemical resistance and great long-time stability. Thus, the new HOIFs must significantly outperform the established ferroelectrics when envisioning their application in various ways in devices. In addition to the rapid development in the HOIFs research field, we now realize that the ultimate trend of miniaturization in electronics has reached its limits. Further scaling down of any electronic element is an extremely challenging task. Evidently, the devices are becoming increasingly smaller and embed more functionality. A unique way to continue the trend defined by increasing product performance without further miniaturization is either to use new, efficiently, and judiciously

designed molecular HOIFs or to improve the known and envisage novel properties of existing HOIFs to bring plentiful and scalable functional applications for existing devices.[23-31] Considering this, the long-term stress tolerance of the flexible hybrid framework is one of the most important challenges for future progress in this field. The mechanical properties of HOIFs, particularly their response to hydrostatic pressure and directionally-induced stress, are practically important for device manufacturing and durability.[31-36] The ultimate goal of subjecting these materials to high pressure is to improve their properties and functionalities for specific applications in photovoltaic and optoelectronic devices. Following that, it remains a frontier challenge to precisely control both the assembly of the molecular building blocks of HOIFs hindered by targeted manipulation with hydrostatic pressure and to test the limits of their mechanical flexibility and tunability. Indeed, pressure is expected to be an effective and clean tool for tuning the flexible structure (*i.e.*, adjusting interatomic distances and bond lengths) and, subsequently, the electrical and magnetic properties of HOIFs. As they are relatively soft and flexible, applying external hydrostatic pressure to HOIFs may induce reversible, irreversible, insulator-to-metal, and crystalline-to-amorphous transitions and stress-activated color changes. These transitions can cause drastic and tunable changes in functional properties, which can lead to intriguing salient points such as metallization and band gap modulation. In their review paper, Lü *et al.* [2017][37] trace the progress in high-pressure research on hybrid framework materials and discuss the effects of pressure on the structures and optical and electrical properties, their relationships, and the underlying mechanisms. Hybrid perovskites, especially those containing non-environmentally friendly lead, are among the most popular materials for high-pressure research due to their high performance for energy-related applications. They systematically exhibit some common features under high pressure, such as, (*i*) pressure-induced amorphization under elevated pressure; a reversible amorphous to crystalline

phase transition when the pressure is released; (*ii*) pressure-induced PL changes are similar, with bond contraction broadening the bandwidths, resulting in a red shift, while increased polyhedral distortion and tilting at higher pressures results in a blue shift; (*iii*) when the pressure exceeds a certain threshold, the intensities of PL generally become weaker and eventually undetectable - the peaks of PL reappear after decompression. In contrast, to these predominant properties, hybrid perovskites exhibit different behaviors, such as (*i*) the variation of intermediate high-pressure phases, (*ii*) the uncertainty of pressure-induced changes in conductivity.[38-41]

Intrigued by the delicate magnetodielectric effect in hybrid organic-inorganic molecule-based improper ferroelectric, triethylmethylammonium tetrabromoferrate(III) with a polar, non-centrosymmetric and non formate-based perovskite-like architecture, that can be readily prepared by a cheap, wet-directed approach. It is expected that probing its mechanical response to external stimuli, such as pressure, will provide a solid platform for the rational development of (for example) sensing and memory devices, where sensitivity to external mechanical stimuli and reversibility are highly desirable. Namely, Xiong *et al.* (2012) significantly expanded the limited number of multiferroic compounds by discovering that the above-room-temperature molecular improper ferroelectric, triethylmethylammonium tetrabromoferrate (III), ($[N(C_2H_5)_3CH_3][FeBr_4]$) exhibits strong magnetodielectric coupling with a magnetodielectric ratio (18% at 0.6 MHz) at approximately the ferroelectric phase transition temperatures ($\approx$360 K).[23] Moreover, the significance of this is also shown by the fact that the magnetodielectric effect in most inorganic-organic hybrid multiferroic materials (regardless of structure) is very weak (less than 1%) and occurs at the onset of magnetic phase transitions. An additional ferroelectric-ferroelectric phase transition at the low temperature of 6*mm*F6 Aizu notation and small magnetic and dielectric anomalies at 171 K also enrich the magnetoelectric functionalities of this multiferroic material.

In this comparative study, we spotlight reversible pressure-triggered mechanochromic features manifesting through a structural transition and a tunable band gap evaluation of magnetodielectric molecule-based hybrid multiferroic, triethylmethylammonium tetrabromoferrate(III), **EMAFB** – using *in situ* characterization measurements performed under mechanical compression responsive conditions, *i.e.*, Synchrotron Powder X-ray Diffraction (SPXRD) experiments, Raman data acquisition, absorption and emission spectroscopy, electrical transport and magnetization measurements. Herein, we have independently encoded experimental evidence for the strict structural symmetry requirements for fragile ferroelectricity leading to a polar-noncentrosymmetric ($P6_3mc$) to polar-noncentrosymmeteric phase transition ($P112_1$; the non-conventional 'unique axis *c*' notation helps to easily represent the symmetry evolution of **EMAFB** *vs*. the increasing pressure). A pictorial transition from hexagonal symmetry to monoclinic topology at relatively low pressure tailed by a gradual color change, discloses subtle alterations in the electronic landscape leading to a striking band narrowing. Moreover, the observed behavior of Pressure-Induced Emission Enhancement (PIEE) and the possibility of tuning the photophysical properties of **EMAFB** and its correlation with the underlying crystal structure are highly desirable steps. The pressure tuning of the structure-property relationship in **EMAFB**, redevelops the field of HOIFs, by modulating the multifunctional integration of significantly different physical properties and the photophysical nature of **EMAFB**, which provokes an interesting roadmap for the development of a high-precision pressure sensing technology of intertwined and merging ferroelectric features suited for different measurement ranges or operating pressures, greatly expanding and updating the physical scenario of the burgeoning HOIF field in general.

EXPERIMENTAL DETAILS

Synthetic Procedures. All the chemicals were purchased as reagent grade from commercial vendors and used directly without further purification. Triethylmethylammonium tetrabromoferrate(III) ($[N(C_2H_5)_3CH_3][FeBr_4]$) (**EMAFB**) was synthesized according to the literature by a method similar to the previous work of Xiong *et al.* [2012][23] by mixing aqueous solutions of anhydrous iron(Ill) bromide ($FeBr_3$; Alfa Aesar, 98% purity, 0.59 g, 2 mmol) and triethylmethylammonium bromide ($(C_2H_5)_3N(Br)CH_3 \cdot H_2O$; TCI Chemicals, 97% purity, 0.30 g, 2 mmol). The solution was stirred for 2 h at room temperature (RT) before being filtered. Within 3 weeks of slow evaporation at RT, blocky, brittle single crystals of mandarin orange color were formed from the salt solution. Some single crystals were extracted from the supernatant, washed with ethanol, and dried at RT, while the rest of the precipitates were ground to a fine powder.

Pressure-induced Synchrotron Powder X-ray Diffraction (SPXRD) measurements. *In situ* high-pressure SPXRD data were conducted at RT up to the experimental limit of 25.9 GPa in axial geometry, using the high-resolution powder diffractometers at beamline 13-BM-C, GSECARS of the Advanced Photon Source (APS), Argonne National Laboratory (ANL), USA (λ = 0.434 Å). The focused beam was about 15 μm in diameter, and the pressure on the DAC was generated using a membrane gas control system. The finely-ground polycrystalline sample of **EMAFB** was loaded into the DAC with 300 microscopic weak fluorescent anvils. The Si oil was used as the pressure-transmitting medium (PTM), and each pressure point was determined by matching the pressure shift of the ruby fluorescence line. In the case of the SPXRD data (as well as the laboratory data) collected at ambient conditions, the *ab-initio* structure solution process was successfully performed by EXPO2014[42] to locate the inorganic anion correctly. As the positions of the Fe and Br atoms are very similar to the corresponding ones of the published structure (solved by single

crystal data)[23], the organic cation determined by powder diffraction data was extremely disordered. For details on the SPXRD experiments, data analysis, and the magnetization measurements under high pressure, please refer to the Supporting Information file.

Pressure-induced Raman spectroscopy. Raman measurements were performed on a MonoVista CRS+ system (Spectroscopy & Imaging) with laser excitation of 532 nm and 633 nm (0.23 mW and 0.5 mW laser power, respectively). Two successive cycles of Raman spectroscopy measurements with pressure increase/release were performed with laser excitation of 633 nm and 0.1 mV power. A grating of 300 and 2400 grooves/mm was used throughout the experiments, and the laser beam spot size was 20-30 μm. Small pieces of single crystal **EMAFB** were loaded into a DAC with 300 μm culet-sized low-fluorescent anvils together with a ruby sphere. The Si oil was used as a PTM. Each pressure point was determined by the fitting pressure shift of the ruby fluorescence line.

Pressure-induced absorption spectroscopy. UV-vis absorption and optical image measurements were performed using an *in situ* high-pressure optical property measurement system developed in-house, a Gora-UVN-FL integrated microdomain spectroscopy system (Ideaoptics, Shanghai). A single crystal **EMAFB** was loaded into the sample chamber along with a ruby sphere, and Si oil was used as the PTM. Each pressure point was determined by the fitting pressure shift of the ruby fluorescence line. UV-vis absorption spectra were collected using a Xenon light source (focused beam size diameter 30 μm) between 300 nm and 1100 nm. The band gap was determined by extrapolating the linear portion of the $\alpha^{1/2}$ *vs.* hv curve, where v is the absorption coefficient, h is Plank constant, and v is the frequency of the photon. All data were collected at room temperature.

Transport measurements under high pressure. Electrical resistance measurements were carried out using the four-probe resistance method. A thin cubic BN layer was inserted between the steel gasket and diamond anvils to insulate the metal gasket from the sample. Four platinum wires were arranged to contact the sample surface in the chamber. A Keithley 6221 current source, 2182A nanovoltmeter, and 7001 switch systems were used as the current supply, voltmeter, and voltage/current switcher, respectively. Experiments were carried out without a PTM, and the sample chamber was filled with a small quantity of crystalline powder **EMAFB**. The electronic transport properties under high pressure and low temperature were studied using van der Pauw's electrical conductivity method in a symmetric DAC. The pressure was generated by a pair of diamonds with a 300 μm diameter culet. A rhenium gasket was pressed, and a hole was drilled into the center of the gasket. An insulating layer of cubic boron nitride (c-BN)-epoxy protected the electrode leads from the metallic gasket. A 150 μm diameter hole was drilled into the center of the c-BN as a sample chamber to place the powdered **EMAFB**. Four platinum strips were arranged to touch the sample in the chamber. Experiments under different pressure-temperature conditions were performed using a laboratory-designed electrical transport system (with optical window) using a Keithley 6221 current source, a 2182A nanovoltmeter, and a 7001 switching device as the current source, voltmeter, and voltage/current switch, respectively. Liquid nitrogen was used to cool the sample. The pressure in the sample chamber was measured using the ruby and diamond fluorescence method.

RESULTS AND DISCUSSION

Structural evolution under pressure at room temperature. The a*b-initio* structure solution from PXRD data collected at ambient conditions (laboratory and synchrotron data) was successfully performed by EXPO2014[42], a package able to carry out all the main steps of the process, *i.e.*, unit

cell determination, space group identification, full pattern decomposition, structure solution, structure model optimization, and Rietveld refinement. The EXPO2014 outcomes were similar to those reported in the literature[23]: EXPO2014 could correctly find the unit cell parameters and the space group and accurately locate the heavy atoms. Attempts to complete the crystal structure by positioning the missing light atoms (non-hydrogen atoms only, to reduce the number of degrees of freedom) were carried out by applying the Simulated Annealing (SA) procedure implemented in EXPO2014. At the end of the SA runs, the organic component of the most plausible structure model was disordered and only partially overlapping the corresponding light atoms of the published structure[23] (see Figure S1 and additional details in the Supplementary Information). Indeed, due to the rough location of the organic cation, we used the literature structure model[23] as a starting model to perform the Rietveld refinement step at ambient conditions before applying pressure. The PXRD pattern of **EMAFB** measured at RT was indexed to a polar, non-centrosymmetric hexagonal $P6_3mc$ unit cell with a $6mm$ point group whose symmetry elements matched those of Xiong et $al.$[23] (Rietveld refinement results: $a = 8.2461(3)$ Å, $c = 13.525(6)$ Å, $Z=2$, $V = 796.5(1)$ Å^3, $R_{wp} = 7.03$ %), as shown in Figure 1a and Table 1. There was no evidence of other phases forming besides the hexagonal **EMAFB** phase, which had a typical six-fold symmetry of a slightly distorted trigonal pyramid, where the $[FeBr_4]^-$ anion mold into the architecture of a completely disordered cationic moiety, within the **EMAFB** crystal lattice. The resulting structural parameters of **EMAFB** at ambient conditions are summarized in Table 1, along with the reliability factors that confirm the validity of the refinement.
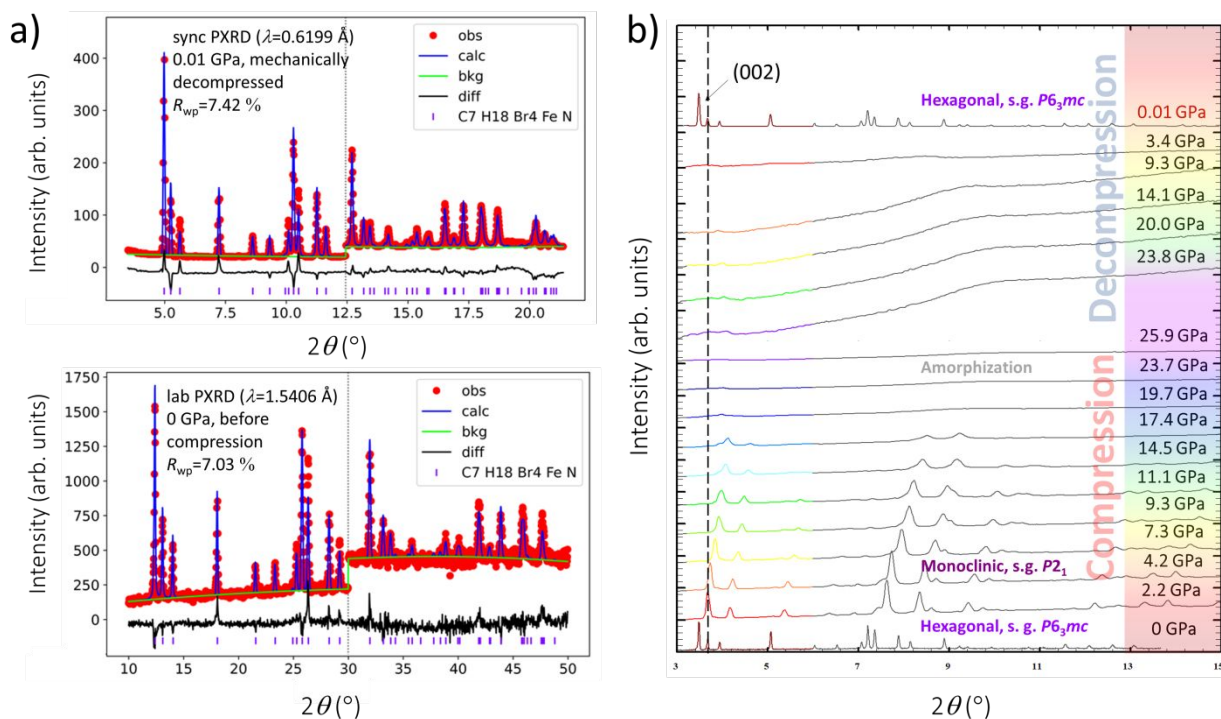
Figure 1. a) Observed (red circles) and calculated (solid blue line) PXRD profile obtained from the Rietveld refinement against the PXRD data of **EMAFB** at ambient conditions before compression (bottom) and the Le Bail fitting following gradual release to 0.01 GPa (top). The difference profiles are depicted by the lower solid black line, and the purple tick marks show the reflection positions of **EMAFB**. The lower solid green lines represent the fitted background contribution. For clarity, the diffraction patterns at the bottom and the top are enlarged twice from 30 to 50° 2θ and from 12.4 to 21.4° 2θ, respectively. **b)** The synchrotron PXRD evolution patterns at selected pressure points compared to the laboratory PXRD data collected at ambient pressure illustrate reversible hexagonal-to-monoclinic phase transformations prevailing the amorphous state. The cascading PXRD patterns are offset for clarity. The value on the right side of each diffraction pattern is the pressure in GPa.

The relatively moderate pressure of 4.2 GPa induces a transition to a completely new phase (see Figure 1b), indexed in the monoclinic system, a primitive unit cell with lattice metrics (a=7.891(2), Å, b=7.156(1) Å, c=12.532(3) Å, γ=111.46(3)°, V=111.46(3) Å^3). The systematic absences suggest, as most likely, a polar, non-centrosymmetric, chiral space group $P2_1$ (C_2^2, Laue symmetry: 2/m, unique axis c (*i.e.*, $P112_1$) (see Figure 2). To describe the symmetry changes induced by the pressure, we adopted the non-conventional monoclinic c setting. The space group $P6_3mc$ comprises mirror planes, its structure is not chiral, and therefore, it lacks an absolute configuration in the ambient pressure phase. In contrast, the space group $P2_1$ has a twofold screw operation, consisting of both rotations by 180° and translations by half a pitch along the screw axis, yielding an identical 2_1 assembly. However, it is a subgroup of the space group $P6_3mc$ belonging to the Sohncke space groups. Normally, for conventional ferroelectric phase transition at ambient pressure, the high-temperature paraelectric phase (centrosymmetric) transforms to the low-temperature ferroelectric phase (noncentrosymmetric), resulting in symmetry breaking.[43] Under hydrostatic compression, ferroelectricity is often inhibited because the short-range repulsions favoring the nonpolar phase grow faster than the long-range interactions favoring the ferroelectric phase. Despite the fact that ferroelectric transitions with symmetry change from noncentrosymmetric-to-noncentrosymmetric do exist, only a few examples of hybrid perovskites such as [NH$_4$][Zn(HCOO)$_3$][44] or (thiazolidinium)CdBr$_3$[45] have been reported to feature such a transition. However, given the structural complexity of polycrystalline samples and the limited data available for high pressures, the assignment of a pressure-induced non-centrosymmetric (even monoclinic) structure still remains rather unclear. In the pressure-driven polar-noncentrosymmetric-to-polar-noncentrosymmetic phase transition of **EMAFB** from a hexagonal to a monoclinic setting at 4.2 GPa, the spatial symmetry operations decrease from 12 to 2. It is

very likely that the movement and/or reorientation of the triethylmethylammonium cation ($[N(C_2H_5)_3CH_3]^+$) and $[FeBr_4]^-$ anion that both lie on the hexagonal axis of the flexible $P6_3mc$ crystal packing show a switchable hexagonal-to-monoclinic phase transition. Namely, the degree of distorted trigonal pyramid tilting increases with increasing pressure because the templated $[N(C_2H_5)_3CH_3]^+$ cations are more compressible than the $[FeBr_4]^-$ polyhedra. This type of transition is reminiscent of the switchable ferroelastic symmetry change observed in temperature-induced measurements of a perovskite-like metal-organic framework, $[Et_4N]_2[PbBr_3]_2$.[46] There, the crystal system changes from the hexagonal $P6_3/mmc$ to the monoclinic $P2_1/c$ setting during cooling, showing a reversible structural phase transition with the Aizu notation of $6/mmmF2/m$. Also, the origin of the phase transition that we observed is similar to that described previously by Fu and Ye (2017). It is due to the movement or reorientation of the organic cations having the ability to buffer compressive stress in the hybrid system and the displacement of the metal and halogen ions in the solid-state crystal.[47,48] A striking feature of ferroelastics is their spontaneous deformation, which can change when mechanical stress is applied and occurs when the material has two or more orientation states that share identical crystal structures when no mechanical stress is applied. When mechanical stress is applied, one of these states is preferred, and a transition from one state to the other occurs. Because of the simultaneous stress and spontaneous polarization, such materials are often used in systems where elastic energy must be converted to electrical energy and vice versa.[49] Understanding the elastic characteristics of molecular multiferroics is critical for their future use because these parameters dictate their durability and reliability in devices. Up to 16.1 GPa, the monoclinic phase was preserved, and no significant symmetry alternations were seen in the SPXRD patterns, except for the shift to a high 2θ value gradually with increasing hydrostatic pressure, suggesting decreasing interplanar spacing and a corresponding contraction of the unit

cell. For any kind of technological development, the elastic properties of molecular ferroelectrics, and in particular, of potential molecular multiferroics, such as triethylmethylammonium tetrabromoferrate(III) are of great importance, since they can determine the durability and reliability of the devices during operation.[50-52] Still, there are virtually no studies analyzing the elastic properties of molecular ferroelectrics of this type. Exceptionally, only a few investigations have comprehensively addressed the elastic properties of molecular perovskite ferroelectrics.[30,53] Nevertheless, a complete ferroelectric/ferroelastic 2F1-type phase transition was studied in depth by Xiong and Zhang (2022).[54] However, considering the extinction conditions for the non-conventional $P112_1$ space group and the successive Le Bail intensity extraction runs of cell parameters (found complementary by both N-TREOR09[55] and DICVOL[56] in EXPO2014, in the 2θ range $2.12° - 20.40°$) in GSAS2, a simple point-by-point mapping of the observed powder pattern intensities to each reflection yields an increasingly improved reflection estimate indicative of the flexible change in the length of the crystallographic axis (Figure 2a). This is consistent with the basic idea that every system has a set of principal axes along which the material reacts linearly, either expanding or contracting, with the response along other directions at the same time conforming to the rule that the largest axis is the one corresponding to the axis of symmetry (*i.e.*, the *c*-axis in the case of the monoclinic cell). This tendency ensures that in all cases, the contraction has a monotonic effect on the principal axis of symmetry, and in the case of monoclinic cells, the contraction of axes *a* and *b* will always be slightly anisotropic. Table 1 lists the unit cell parameters resulting from a) the Rietveld refinement of **EMAFB** at ambient conditions (prior to application of pressure), b) the Le Bail fitting of the SPXRD high-pressure data with respect to $P112_1$ space group, and c) the Le Bail fitting of the powder pattern of the relaxed **EMAFB** sample (0.01 GPa data).

Table 1. Summary of **EMAFB** unit cell metrics and reliability factors obtained from the Rietveld refinement of laboratory PXRD data ($\lambda^a = 1.54056$ Å) collected at ambient conditions and Le Bail intensity extractions of high-pressure SPXRD data ($\lambda = 0.434$ Å and $\lambda^b = 0.6199$ Å) at RT. The Le Bail fitting against synchrotron PXRD high-pressure data are shown with respect to the $P112_1$ setting.

P (GPa)	a (Å)	b (Å)	c (Å)	α (°)	β (°)	γ (°)	V (Å^3)	s.g.	R_{wp}
0.0^a	8.2461(3)	8.2461(3)	13.525(6)	90	90	120	796.5(1)	$P6_3mc$	7.03
2.2	7.946(1)	7.946(1)	13.040(5)	90	90	120	712.9(2)	$P6_3mc$	5.13
3.7	7.7908(6)	7.7908(6)	12.769(3)	90	90	120	671.2(1)	$P6_3mc$	2.68
4.2	7.891(2)	7.156(1)	12.532(3)	90	90	111.46(3)	658.6(2)	$P112_1$	1.63
5.8	7.373(1)	6.5854(6)	12.484(3)	90	90	91.57(2)	606.0(1)	$P112_1$	1.83
7.3	7.301(2)	6.5250(9)	12.387(5)	90	90	91.81(3)	589.8(1)	$P112_1$	2.19
7.9	7.234(2)	6.4040(7)	12.282(3)	90	90	91.73(3)	568.7(1)	$P112_1$	1.49
9.3	7.161(2)	6.3403(8)	12.178(6)	90	90	91.84(4)	552.7(1)	$P112_1$	1.58
11.1	7.131(3)	6.276(1)	12.096(5)	90	90	91.34(4)	541.1(2)	$P112_1$	1.95
13.1	6.949(3)	6.1979(6)	11.979(6)	90	90	91.63(4)	515.3(2)	$P112_1$	1.79
14.5	6.890(3)	6.146(1)	11.933(9)	90	90	91.60(5)	505.2(3)	$P112_1$	2.27
16.1	6.897(8)	6.105(2)	11.933(9)	90	90	96.6(1)	501.2(6)	$P112_1$	1.43
0.01^b	8.252(1)	8.251(1)	13.544(2)	90	90	120	798.8(2)	$P6_3mc$	7.42

^{a}Rietveld refinement of laboratory PXRD data collected at ambient conditions ($\lambda = 1.54056$ Å).
^{b}The 0.01 GPa pressure point was achieved by releasing screws from the DAC.

The aforementioned deformation puzzle shattered by the structural transition promoted by hydrostatic pressure, reveals the transient dynamic behavior of **EMAFB**. The phase transition from a hexagonal structure to a monoclinic non-conventional $P112_1$ setting caused by the mechanical response of **EMAFB** is clearly reflected in the evolution of the metric and volume of the unit cell (see Table 1).
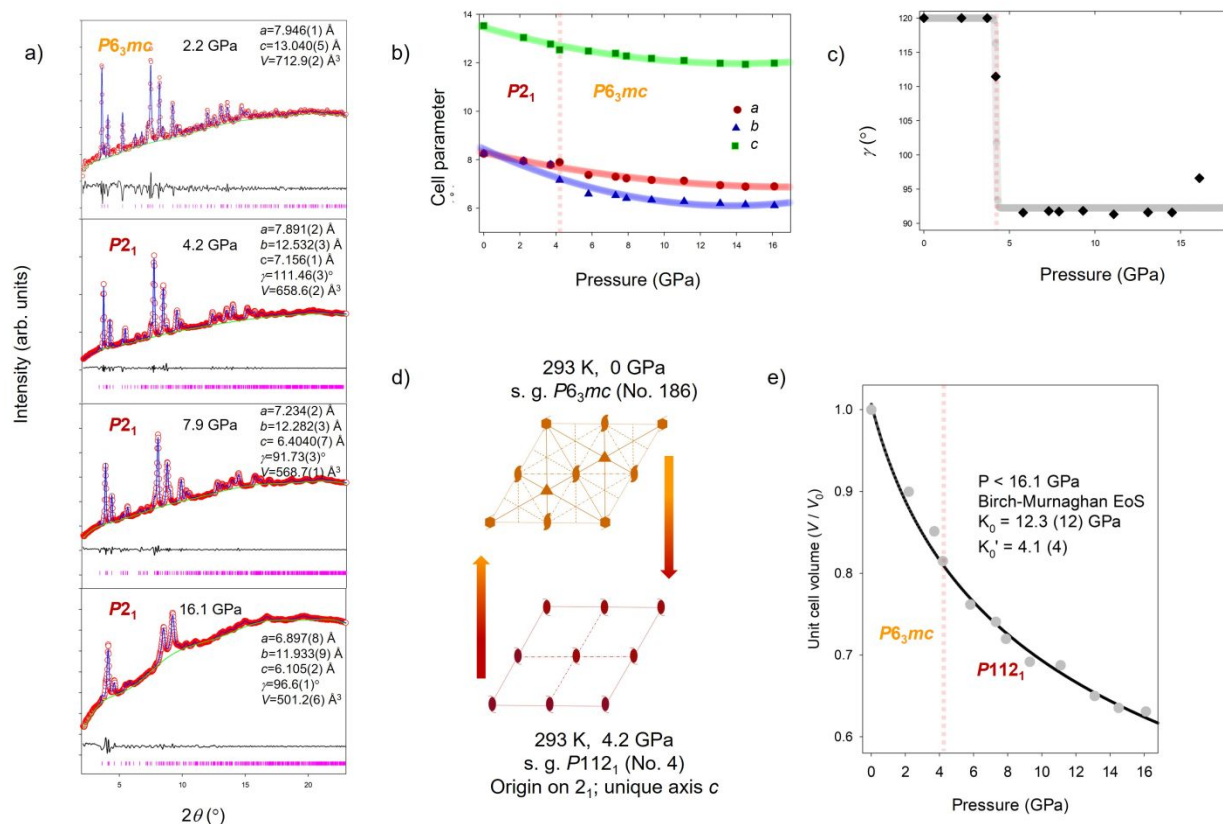
Figure 2. a) The peak intensity extraction cascade mode from an indexed powder diffractogram using the Le Bail algorithm for the selected SPXRD patterns dominated by the $P2_1$ symmetry (λ = 0.434 Å) at RT. The final observed and calculated PXRD profiles from the Rietveld refinement coupled with Le Bail extraction against the **EMAFB** SPXRD data are shown as red dots and solid blue lines, respectively. The fitted background contributions are shown by the lower solid green lines. The lower solid black lines show the difference profiles, while the purple vertical marks indicate the calculated positions of the Bragg peaks. **b)** Evolution of lattice constants of **EMAFB** under compression. **c)** Evolution of lattice angle γ of **EMAFB** under compression. **d)** Schematic projection of the equatorial plane of point groups $6mmm$ in the hexagonal phase and $2/m$ in the monoclinic phase during the structural transition triggered by reversible pressure. **e)** Isothermal (293 K) pressure dependence of unit cell volumes of the monoclinic phase with increasing pressure.

The dashed blue line through the data points is a third-order semiempirical Birch−Murnaghan line EOS. Transparent solid lines (b and c) are guides to the eye, while transparent vertical dashed lines (**b**, **c**, and **e**) represent the onset of the phase transition.

Namely, the volume collapse of the unit cell of ~17.3% at 4.2 GPa reflects the contraction of the *a* and *b* axis for about ~4.3%, and 13.2%, respectively, while the *c*-axis shrinks by almost 7.4%. Accompanied by the overall ~37.1% volume reduction under increasing hydrostatic pressure, the *b*-axis undergoes a pronounced ~26% reduction. The *a*-axis and *c*-axis are compressed similarly, by nearly 16.4% and 11.8%, respectively, at 16.1 GPa (see Figure 2b). Such behavior is very likely triggered by enhanced flexibility of the triethylmethylammonium tetrabromoferrate (III) framework assembled via the organic skeleton, particularly, the pressure-induced intermolecular H-bond interactions[57]. An important change also occurs in the monoclinic γ angle when the pressure is increased to 7.9 GPa. Namely, the γ angle drops sharply from 120° at 0 GPa to 111.46(3)° at 4.2 GPa, then drops further to 91.57(2)° at 5.8 GPa, and then alternately rises and falls in small increments to finally reach 96.6(1)° at 16.1 GPa (Figure 2c). At pressures greater than 16.1 GPa, there is a relatively sharp decrease in diffraction intensity, as evidenced by the appearance of a broad diffuse background, indicating the onset of abrupt amorphization. Still, some peaks of crystalline hybrid are preserved even at relatively higher pressure. In particular, the highly broadened (020) and (-222) Bragg reflections related to the long-range packing of the $[FeBr_4]^-$ anion in the unique-axis *c* setting of $P112_1$ can be observed up to 19.7 GPa (see Figure 1b). Therefore, the stress-activated amorphous sample should retain the cross-linked, tilted $[FeBr_4]^-$ anion and highly deformed $[N(C_2H_5)_3CH_3]^+$ cation. Given that the crystal structure consists of an inorganic skeleton and organic fillings with different bond strengths, the pressure-driven gradual structural distortion and amorphization are not surprising but sufficiently

compelling. Similar pressure-triggering effects have already been reported for organic molecular ferroelectrics, and organohalide perovskites, systems that exhibit highly tunable electronic structure, with band gaps in the visible range, followed by piezochromism.[38,39,58-61] However, the amorphous phase returns to the original hexagonal symmetry when the pressure is mechanically released from the highest applied pressure to 0.01 GPa. The pressure-treated sample recovers completely and exhibits structural stability followed by nearly the same unit cell metrics as before compression (see Figure 1a). Such a specific trend of pressure-induced recrystallization is uncommon. For example, Zhao, Xu, Kanatzidis, and Jia *et al.* (2016)[41] reported that the diffraction peaks of the decompressed $CH_3NH_3SnI_3$ perovskite are broadened compared to those of the initial sample, which is likely due to the combined effect of the size reduction of the perovskite grains and the increased local strains between them after compression. This confirms a memory effect commonly attributed to the elasticity of the hybrid organic-inorganic framework that serves as a "template" for the recrystallization process. The phase transition caused by the mechanical compression of **EMAFB** (Figure 2d) is clearly reflected in the evolution of the unit cell metrics and volume, as can be drawn from the data listed in Table 1 - the collapse of the volume of the unit cell from hexagonal to monoclinic by ~37% at 16.1 GPa reflects experimental pressure-volume data. The calculated compressibility parameters of the monoclinic phase $K_0 = 12.3(12)$ GPa, $K_0' = 4.1(4)$ (Figure 2e) show a trend that can also be observed directly in hybrid perovskites.[58,61,62] However, the low value of the bulk modulus is comparable to values typical of HOIFs such as $[CH_3NH_3]PbI_3$ ($K_0 = 10.4$ GPa),[63] $[CH_3NH_3]SnI_3$ ($K_0 = 12.3$ GPa),[41] and $[(NH_2)_2CH]PbI_3$ ($K_0 = 11.8$ GPa)[64] where the metal center and thus, the strength of the coordination bond typically determines the mechanical response of such materials. If the calculated bulk modulus is compared to those of typical oxide ferroelectrics, such as $BaTiO_3$, $Pb(Zr_{1-x}Ti_x)O_3$, or

$KNbO_3$, whose bulk moduli are frequently over K > 100 GPa,[65] the difference in the bonding situation and physical density becomes clear, which in turn demonstrates the highly compressible nature of **EMAFB**, *i.e.*, poor pressure resistance and softness. Broadly speaking, the calculated bulk modulus of **EMAFB** is much lower than that of oxide perovskites indicating the soft nature of this hybrid and strong structural change at relatively low pressure. It is advantageous for the development of the band gap and, in particular, for the realization of the hybrid material in which excellent piezoelectric performance and mechanical softness can coexist, bridging the design space that spans those of "soft" piezoelectric biosystem/polymer materials and "hard", conventional high-performance piezoelectric ceramics smaller.[66]

Fingerprint spectral region screening by pressure-driven Raman measurements. To support our interpretation, in addition to XRD characterization, which serves as a guiding principle for distinguishing crystal forms, solid-state Raman band assignments can capture the smallest differences in energies of the external and internal crystal lattice vibrational modes, which are affected by changes in molecular interactions. Because the external vibrational modes in the low-frequency region of the Raman spectrum are particularly sensitive to crystal form and molecular arrangements within the unit cell, the merit of the Raman signature consequently complements the XRD features by depicting details of the observed structural alterations. The local structure modifications under compression of **EMAFB** were traced by collecting Raman data at ambient conditions (Figure 3a) and across the elevated pressure points up 8.2 GPa (Figure 3b and c) and up 32 GPa (Figure 3f) focusing on the subset vibrations of the low-frequency region. Figure 3a shows the Raman spectra of the single-crystal **EMAFB** at ambient conditions observed with a 633 nm laser excitation wavelength. A close-up view of the low-frequency region (Figure 3b) depicting cascade Raman data up to 8.2 GPa obtained during compression shows bands arising from only

two of the four Raman-active fundamentals of the low-frequency $[FeBr_4]^-$-containing modes, $v_1(\alpha_1)$ and $v_3(\tau_2)$ at ~202 cm^{-1} and 293 cm^{-1}, respectively.[67,68] In particular, the low-energy lattice modes are sensitive to crystal structure alternations, and any change in this region can be directly linked to local structure modifications, consequently leading to phase transitions.[58,69,70] A gradual shift of only three Raman modes can be followed during compression with a 633 nm laser since the intensities of the other peaks are too low to fit the peak position accurately; the stronger mode is due solely to the $v_1(\alpha_1)$ fundamental, while the other emanates from a combination of the $v_1(\alpha_1)$ fundamental and one or both τ_2 fundamental modes, one of which can only be distinguished below 100 cm^{-1}. Above 6.0 GPa, the laser-induced fluorescence emission rapidly increases and completely obscures Raman modes above 8.2 GPa.
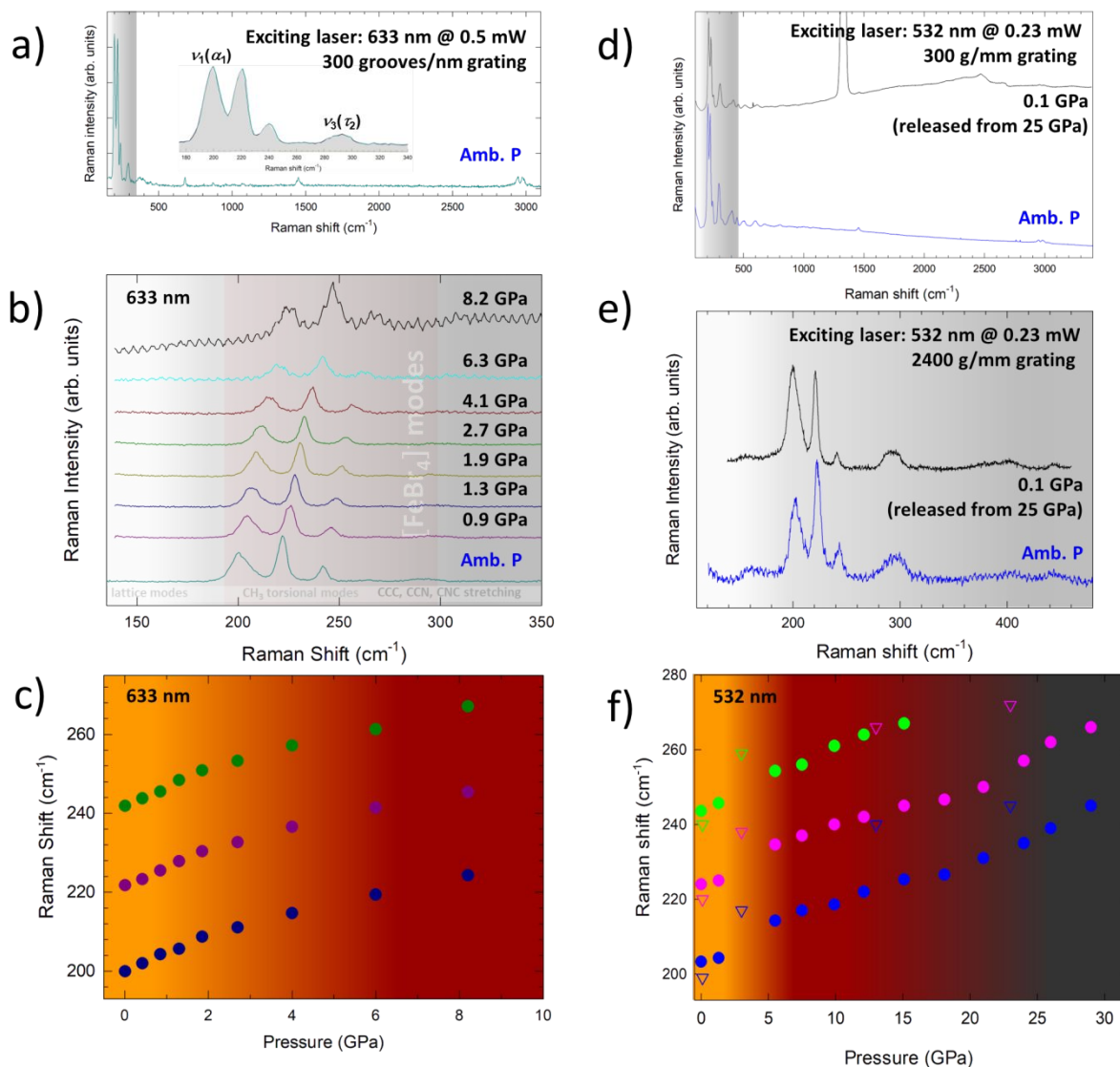
Figure 3. Raman spectra of single-crystal **EMAFB** obtained by a (**a** and **b**) 633 nm and (**d** and **e**) 532 nm laser source. The pressure dependence of Raman peak frequencies at various pressure points in the low-frequency region obtained by (**c**) 633 nm and (**f**) 532 nm laser. Colored backgrounds in **c)** and **f)** are guides to the eye, where the mandarin orange = $P6_3mc$ space group, the maroon and reddish brown = $P112_1$ space group, and the black= amorphous phase. Inset in **a)** shows a close-up view of the low-frequency region.

Figure 3c depicts the pressure-dependent peak frequencies of the observed Raman modes. Namely, the pressure shifts of these modes are sensitive to the intermolecular distance decreases and exhibit rapid shifts in the low-pressure range (4.7 cm^{-1}/GPa up to 1.9 GPa), while smaller shifts are observed above 1.9 GPa (2.4 cm^{-1}/GPa). Such a slope change indicates the structural change triggered by increasing pressure. This agrees quite well with the results for reduced-dimensionality perovskites [Wang and Zou, 2020][58] as all modes shift significantly to the blue upon compression, indicating that the intermolecular vibrational frequency increases significantly, likely due to the reduction in interlayer spacing during the compression process. In the second run, a 532-nm laser (see right column in Figure 3d-f) was used to observe the obscured Raman modes above 8 GPa, and we could trace the peaks up to 32 GPa. The Raman modes showed a continuous shift up to 32 GPa, but above 23 GPa, a rapid broadening of the peak starts, where the intensity decreases rapidly. The broad and weak *in situ* high-pressure Raman spectra of **EMAFB** are unambiguously related to the local structural distortion[36] of the organic template and inorganic polyhedra. All Raman modes disappear above 32 GPa, which indicates their amorphous character. Surprisingly, the Raman modes reappear at 23 GPa upon decompression from 35 GPa, and an almost complete restoration of the spectrum to the original state was observed at 0.1 GPa, providing another salient feature in the excellent agreement with the PXRD results. The reproducibility was confirmed by two consecutive cycles of Raman spectroscopy measurements on the **EMAFB** sample (Figure 4, Table S1). In the first cycle, the sample was compressed to ~30 GPa (see 1P28 pressure point in Figure 4), resulting in amorphization, but also in the recovery of crystalline form after the DAC was decompressed to 0.01 GPa (1PR35 pressure point in Figure 4). The use of a 633-nm laser with a power of 0.1 mW allowed the finer scaling of the data in the low-frequency region (< 200 cm^{-1})

associated with the lattice mode vibrations, in particular, with the $\nu_4(\tau_2)$ low-frequency $[FeBr_4]^-$-

containing fundamental mode at ~100 cm^{-1}.
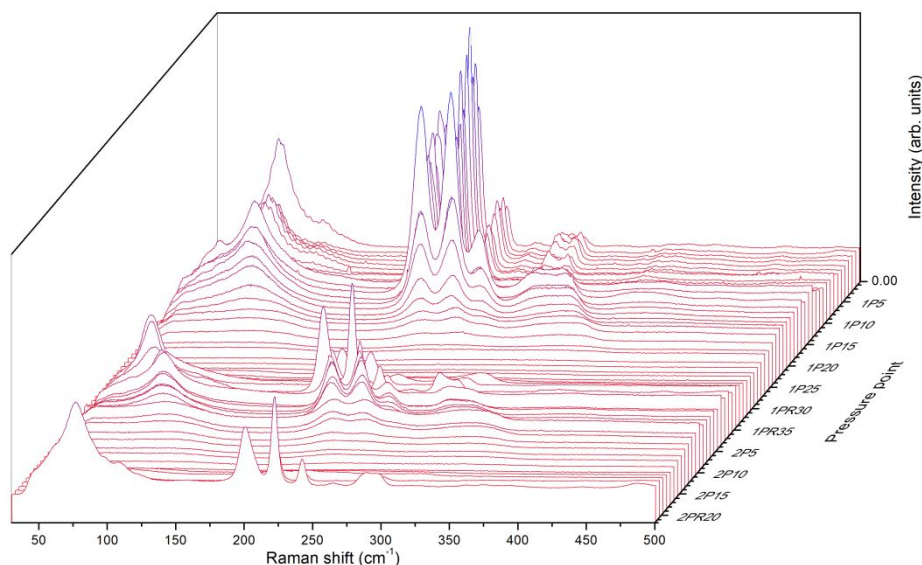
Figure 4. Two consecutive cycles of *in situ* Raman spectroscopy measurements on the **EMAFB** according to the data listed in Table S1.

After depressurization to ambient conditions, the same DAC was fully pressurized to ~36 GPa (2P17 pressure point in Figure 4) and released to 0.01 GPa (2PR21 pressure point in Figure 4). After the second cycle, the **EMAFB** returned to crystalline form, accompanied by a reversible color change (in both runs). The change in the dynamic states of the cations entails a change in the symmetry of the polycrystals, leading to the formation of the polar non-centrosymmetric phase above ambient pressure. To investigate the mechanism underlying the stress-activated color changes (*i.e.*, translucent mandarine orange→ maroon → reddish brown → opaque black), it

seemed obvious to impose the photo responsiveness of **EMAFB** before and after high-pressure

treatments, elucidating another key parameter describing its distinctive characteristics.

Pressure-induced UV-Vis absorption spectroscopy features. Turning attention to the electronic

scenery, the selected absorption spectra upon compression are shown in Figure 5a. At ambient

conditions, a sharp absorption edge is observed at about 540 nm. Upon initial compression, the

absorption edge shows almost no change up to 3.0 GPa and starts a gradual red-shift with further

pressure increase. The UV-vis spectrum above 16.0 GPa exhibits a sharp increase in absorption,

indicating the phase transition's emergence, accompanied with a drastic change in its electronic

landscape. At higher pressure, a broadening and continuous red shift of the absorption edge to

longer wavelengths, eventually covering the entire visible and near-infrared region, was observed.

Above 27.7 GPa, the UV-vis spectra go out of the measurement range for this set-up. The

extraordinary mechanocromic transition of **EMAFB** is accompanied by striking changes in the

optical micrographs (Figure 5b). The pictorial transition from hexagonal symmetry to monoclinic

assembly is triggered by a subtle color change from translucent mandarin orange at ambient

pressure to glassy maroon near 11 GPa, reddish-brown slightly above 12 GPa, turning to opaque

black upon reentry into the amorphous phase region near 20 GPa, before finally returning to

translucent mandarine orange upon decompression. Being compliant to some extent with halide

perovskites results, these pictorial key takeaways provided us with a basic understanding of the

relationship between the crystalline structure and optical properties[38,71,72] as mechanochromic

properties vary in a completely reversible manner, coinciding with changes observed in the PXRD

patterns and absorption spectra. (Figure 1b, Figure S2). Figure 5c shows the evaluation of the

optical band gap as a function of pressure. The optical band gap of **EMAFB** was extracted by

extrapolating the linear component of Kubelka-Munk function plots [F(R)]. At ambient conditions,

the indirect optical band gap was estimated to be 2.3 eV, characteristic of wide band gap semiconductors, and the value does not change up to 3.0 GPa. This fits well with recent research on the extremely narrow band gap observed in the first metal-organic perovskites with piezoelectricity, reported by Zhang and Xiong in 2020.[33] Namely, the (ferrocenylmethyl)trimethylammonium-based inorganic molecular ferroelectrics $(FMTMA)PbI_3$, $(FMTMA)PbBr_2I$, and $(FMTMA)PbCl_2I$ crystallize in the non-centrosymmetric monoclinic polar *C* space group of the 2-point group and exhibit band gaps of 2.37, 2.32, and 2.28 eV, respectively, which are smaller than those of most other lead halide perovskite piezoelectrics or ferroelectrics such as $(CH_3)_3NCH_2I)PbI_3$ (2.82 eV),[34] $EA_4Pb_3Br_{10}$ (~2.70 eV, EA = ethylammonium),[72] (4-aminotetrahydropyran)$_2PbBr_4$ (3.12 eV),[73] and (cyclohexylammonium)$_2PbI_4$ (2.95 eV)[74] and much smaller than those of some inorganic semiconductors, such as Nb_2O_5, ZnO, and GaN (larger than 3.0 eV).[75]
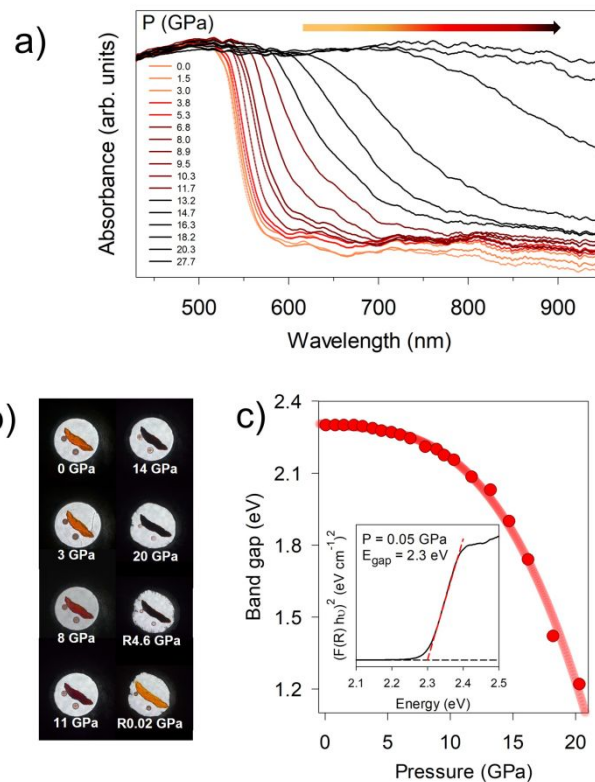
Figure 5. a) Pressure-dependent UV-vis absorption spectra of 1 showing red-shift. **b)** Optical micrographs of **EMAFB** compressed up to 20 GPa and decompressed to 0.02 GPa in the DAC chamber. **c)** Band gap energy evaluation of **EMAFB** with respect to pressure. The inset shows the selected UV-vis absorption spectra at ambient conditions plotted in Kubelka-Munk function. Transparent solid red line is a guide to the eye.

Above 3.0 GPa, the band gap systematically decreases to 15.0 GPa with a closure rate of -33 meV/GPa. Above 15 GPa, the band gap shows a sharp decrease to 20 GPa with a closure rate of -136 meV/GPa, where it reaches our effective measurement range. However, the most striking

finding from the data comparison is that the narrowed bandgap has reached the required upper

theoretical limit for the efficiency of pn-junction solar energy converters upon lattice compression,

since according to the Shockley-Queisser theory,[76] the semiconductor with an optimized bandgap

energy of 1.34 eV is crucial to reach the 33.7% efficiency limit. As pointed out by Wang and Zou

[2019][77], the band narrowing we found (Figure 5c) is most likely due to two competing processes,

namely the tilting of the Fe-Br bond or the reduction of the Br-Fe-Br angle, which directly affect

the optoelectronic properties, increasing the overlap of the metal halide orbitals, and breaking the

Shockley-Queisser limit of 1.22 eV at a relatively moderate pressure of 20.3 GPa. For comparison,

the band gap of $Cs_3Bi_2I_9$ is continuously reduced under high pressure. The optimum band gap was

found to be 1.12 eV at 12.1 GPa, while the pressure-treated $(BA)2(MA)2Pb_3I_{10}$ ($MA = CH_3NH_3^+$,

$BA = CH_3(CH_2)_3NH_3^+$) shows a narrowing of the band gap from 1.94 to 1.78 eV (8.2% decrease),

after compression to 26 GPa and subsequent decompression to ambient pressure.[78] Obviously, the

color properties of **EMAFB** are primarily determined by the charge transfer excitations that govern

the fundamental band gap. Due to the strong Van der Waals forces between the adjacent organic

skeleton and the inorganic cation with sixfold symmetry, and the cooperation of hydrogen bonds,

this structure inevitably exhibits special quantum confinement effects, as shown by the pressure-

dependent PL spectra recorded up to 21.4 GPa (Figures 6a and b). Under ambient conditions,

EMAFB shows no emission, while the intriguing PIEE behavior increased above 8.2 GPa up to

17.3 GPa and then decreased, coinciding with the structural changes (Figure 6a and b). Indeed,

high-pressure SPXRD data have shown that a sudden increase in the degree of structural distortion

(aided by the vibration and distortion of the inorganic polyhedra indicated by the Raman results),

and the enhanced template influence of the light organic cations cause a significant increase in the

electron-phonon coupling energy, promoting the formation and radiative recombination of trapped

excitons,[58,76,79,80] leading to an enhanced PL response at 8.2 GPa. Recent reports have provided more concrete evidence that the PIE is directly affected by the distortion, with the PIE becoming more pronounced the stronger the distortion.[81-83] It cannot be overlooked that coordination bonds, hydrogen bonds, halogen-halogen interactions, and the Van der Waals effect contribute to softer lattices with more active phonon states and a greater role of lattice vibrations. Indeed, the pressure-induced structural amorphization promotes lattice distortion of the original **EMAFB**, increasing the binding energy and the radiative decay of the self-trapped excitons.
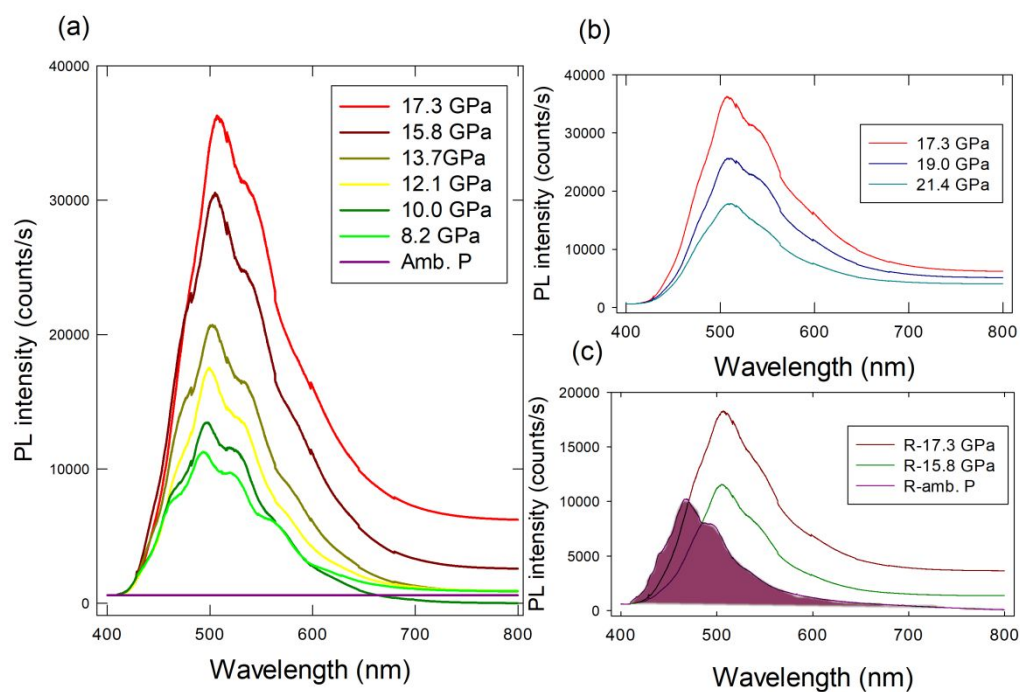
Figure 6. Pressure-induced evolution of PL spectra of **EMAFB** in the pressure range from **a)** ambient pressure to 17.3 GPa, **b)** 17.3 to 21.4 GPa during compression, and **c)** release pressure to ambient. All spectra were obtained using a 405 nm laser as the excitation source.

The pressure-induced suppression effect at PL begins to dominate the emission process above 17.3 GPa (Figure 6b), so the PL attenuation is slow and nonlinear.[58,77] When the pressure is lowered to

ambient, the emission intensity still remains at a multiple of the original value (Figure 6c). Although the hexagonal arrangement of **EMAFB** relaxed to ambient pressure is symmetrically consistent with the original sample, the small difference in the observed diffraction intensities possibly suggests a slight reorganization of the structural units responsible for the emission of the sample decompressed to 0 GPa (*i.e.*, in the case of the 0.01 GPa data we can observe a slight contraction of the cell volume compared with the 0 GPa data, as listed in Table 1). Since the striking pressure-induced optical changes and the pronounced piezochromic features of **EMAFB** indicate significant electronic alternations under compression, we were motivated to evaluate the changes in its electrical transport properties, one of the key parameters for photovoltaic materials.

In situ **high-pressure resistance features.** The electron transport property of **EMAFB** is illustrated in Figure 7, one of the key parameters for semiconductors. The resistance of **EMAFB** sharply decreases by three orders of magnitude at the initial compression (P < 3 GPa) and gradually decreases with further increasing pressure until a peak value is reached at about 16.0 GPa, which then continuously and drastically decreases to reach a minimum value of 4×10^3 Ohm at 80 GPa, indicating the predominant semiconductor character. The broadening of the valence and conduction bands, as well as the shortening of the bonds, favors this behavior.[84,85] This is a much higher value than that reported by Wang and Zou [2018] for the zero-dimensional metal halide perovskite, $Cs_3Bi_2I_9$ where the resistance reaches a minimum value of 33 Ohm at 28 GPa, indicating metallization upon compression.[86] The evolution of the resistance of **EMAFB** over 3 GPa agrees very well with the pressure-dependent evolution of the band gap. Complete closure of the band gap closure and transition from a semiconductor to a metal can be achieved when the pressure is further increased above 100 GPa in a fully amorphous state of **EMAFB**. After depressurization, the enormous resistance of **EMAFB** and the crystal color were recovered at 0.5

GPa, again consistent with PXRD and UV-Vis absorption measurements. The electrical resistivity

of **EMAFB** at 56 GPa not only shows an increase in resistivity upon cooling, but also suggests

that **EMAFB** remains semiconducting at 72 GPa (Figure 7b and c).
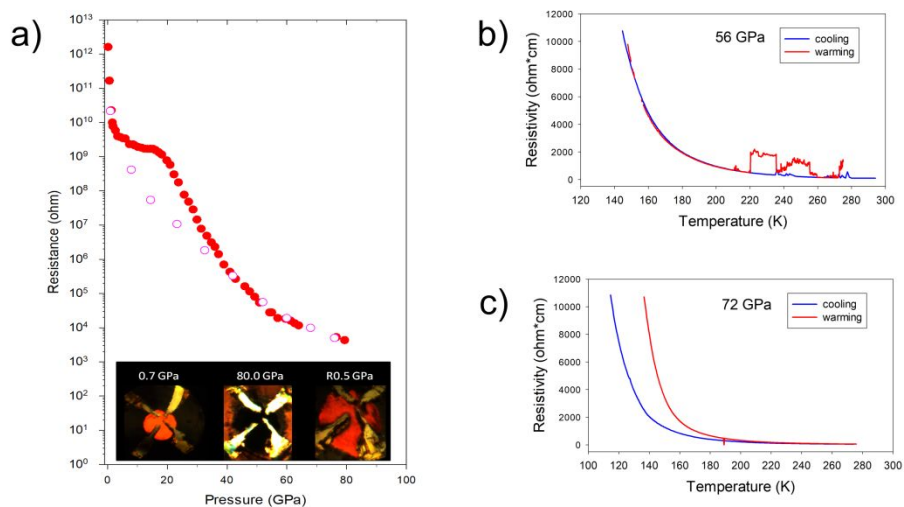

Figure 7. a) Evolution of **EMAFB** electrical resistance during compression (red circles) and decompression (purple outlined circles). Inset: optical micrographs of piezochromic **EMAFB** inside the DAC at two characteristic pressures and after release at RT. The crystal color was fully recovered when the pressure was released. The temperature dependence of the electrical resistivity at **b)** 56 GPa and **c)** 72 GPa.

High-pressure magnetic measurements. The effect of pressure on the magnetic transitions of

EMAFB is shown in Figure 8. Magnetization measurements of a sample marked as "no cell" that

we performed before loading the sample in the pressure cell revealed two distinct anomalies at $T_\uparrow$

= 368.4 K during the increasing temperature and at $T_\downarrow$ = 360 K during the decreasing temperature.

This magnetic feature confirmed a reversible first-order structural transformation between the high-temperature paraelectric and the low-temperature ferroelectric phases.
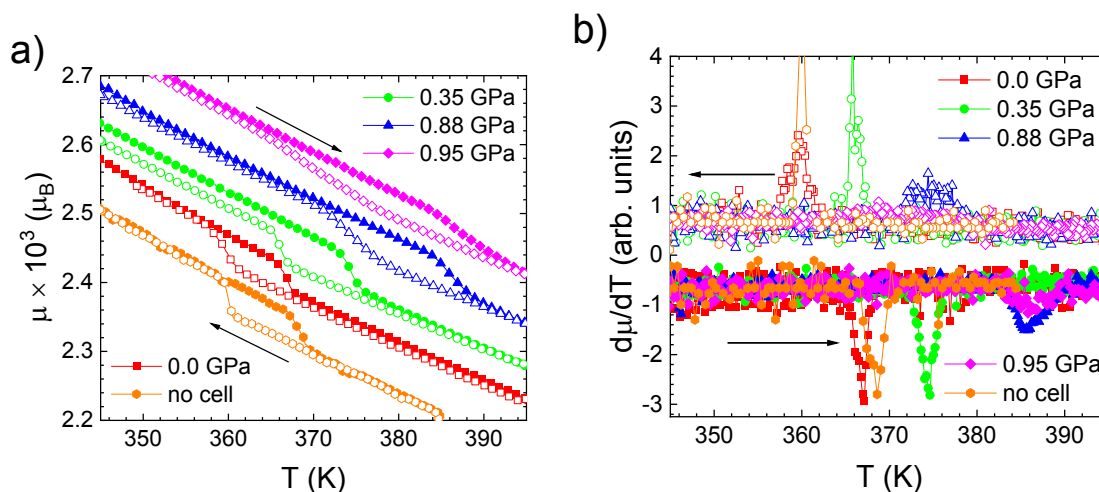

Figure 8. Magnetization measurements of **EMAFB** in vicinity of the phase transition were measured in an applied magnetic field of μ_0H = 100 mT heated (solid symbols) and cooled (open symbols) without a pressure cell ("no cell" data) and in a hydrostatic pressure cell (all other data): **a**) the magnetization data; the data measured in the pressure cell are offset for clarity, and **b**) the derivative of the data from panel **a)**. The arrows indicate the direction of the temperature change.

Our hysteresis interval of 8.4 K is slightly broader compared to the $T_\uparrow$ = 366 K; $T_\downarrow$ = 361 K reported by Xiong *et al.*[23] Applied hydrostatic pressure shifts the $T_\uparrow$ anomaly to higher temperatures with a linear pressure coefficient $dT_\uparrow/dP$ = 19.8 K/GPa to 374.3 K; 385.5 and 386.5 K for 0.33 GPa; 0.88 GPa and 0.95 GPa, respectively. The $T_\downarrow$ anomaly shifts with the pressure coefficient $T_\downarrow/dP$ = 13.4 K/GPa to 366 K, 373.8 K and 371.5 K for 0.33 GPa; 0.88 GPa and 0.95 GPa, respectively. The paraelectric-ferroelectric phase transition was observed at the same temperatures, so these transitions have a multiferroic nature. Pressure release leads to almost complete recovery of the magnetic signal (compare "0 GPa", in which case the sample is in a

pressure cell, and "no cell" data in Figure 8), which is consistent with the reversibility of other

pressure-induced phenomena reported in previous sections. Xiong *et al.* reported a

ferroelectric−ferroelectric phase transition at ~171 K.[23] Our magnetization measurements (see

Figure 9a) show no anomaly at these temperatures, and that is why we conclude that this

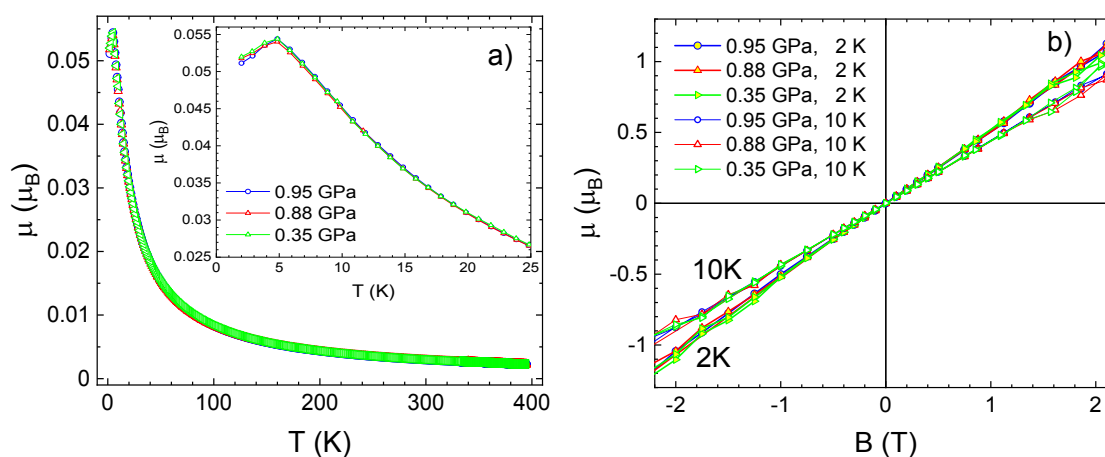ferroelectric-ferroelectric transition has a purely electric nature. It is not connected with the

magnetic structure change.

Figure 9. Magnetization under pressure, **a)** temperature dependence of magnetization ($\mu_0 H = 100$

mT), **b)** magnetic isotherms at different temperatures. For clarity, the data are labeled with the

pressures determined at the $T_\uparrow$ transition. Since the pressure in the clamped CuBe piston cell is

temperature-dependent, the real pressure is estimated to be 0.19 GPa lower.

A maximum at about 5 K is a fingerprint of the magnetic ordering and magnetic isotherms at 2 K

and 10 K (see Figure 8 b), indicating an antiferromagnetic type of ordering. The maximum is at

about 5 K and the magnetic isotherms are intact under pressure.

CONCLUSION

High-pressure research is an intriguing control knob for inducing emergent properties and achieving new functionalities that can greatly improve our understanding of the fundamental science and structure-property relationships of HOIFs. In short, several controllable properties have been proposed upon lattice compression/decompression of selected HOIF, $[N(C_2H_5)_3CH_3][FeBr_4]$, **EMAFB**. With the limited data available due to the influence of pressure on the resolution limits of experiments using a high-pressure DAC design, we have shown that there is a wide range of tunable physical and photophysical properties, that can be dynamically (in a stimuli-responsive and reversible/irreversible manner) controlled by *in situ* high-pressure SPXRD and Raman experiments, absorption and emission spectroscopy, electrical transport, and magnetization measurements. A reversible pressure-induced band narrowing of 1.22 eV at 20.3 GPa satisfying the requirements of Shockley-Queisser theory, and an irreversible PIEE observed above 8 GPa revealed subtle changes in the electronic landscape, with a fully reversible piezochromism from translucent mandarin to reddish brown, and finally to opaque black, systematically closing at a rate of about −136 meV/GPa at 20 GPa. The mechanism underlying the above physical and photophysical features has been shown to be related to the pressure-induced amorphization triggered by the phase transition from hexagonal ($P6_3mc$) to monoclinic ($P2_1$) symmetry. It involves frustrations in the inorganic framework, which is driven by strong interactions with disordered organic cations and the recovery track of the **EMAFB** lattice. Therefore, the soft nature of the environmentally friendly (compared to hybrid organic inorganic perovskites containing lead) **EMAFB** that has been probed by pressure-induced amorphization

and recrystallization, may be advantageous for tuning the band gap, and in particular for realizing

HOIF, in which excellent piezoelectric performance and mechanical softness can coexist. With

resistance dropping to 4 x 10^3 ohms at 80 GPa and retaining its semiconducting character at 72

GPa, this HOIF landmarks the development of technologies that take advantage of pressure-

activated modification of the electronic structure.

ASSOCIATED CONTENT

Supporting Information. This material is available free of charge via the Internet at

http://pubs.acs.org:

- Experimental details on *in-situ* high-pressure SPXRD experiment and data analysis

- Experimental details on *in-situ* high-pressure magnetization measurements

- Pressure-dependent UV-vis absorption spectra

- Pressure points of Raman data collection

AUTHOR INFORMATION

Corresponding Author

*Martina Vrankić - Division of Materials Physics, Ruđer Bošković Institute, Bijenička 54, 10000

Zagreb, Croatia; mvrankic@irb.hr

Author Contributions

M.V. prepared the sample; T.N. performed the high-pressure PXRD, Raman spectroscopy,

transport measurements, and contributed to data analysis; M.V. and Y.D. are responsible for

raising funds; X.L. and K.B. performed the high-pressure UV-vis absorption spectroscopy

measurements and optical image collection; H.L. performed high-pressure SPXRD measurements;

M.V., J.P. and A.M. performed the structural analysis on SPXRD data; Z.J., M.M., and M.M. performed and interpreted the magnetization measurements; M.V. conceived the project and contributed to conceptualization. All authors contributed to the paper, which was written by M.V.

Notes

The authors declare no competing financial interest.

ACKNOWLEDGMENTS

REFERENCES

1. Chang, S.-J.; Chung, M.-H.; Kao, M.-Y.; Lee, S.-F.; Yu, Y-H.; Kaun, C.-C.; Nakamura, T.; Sasabe, N.; Chu, S.-J.; Tseng, Y.-C. $GdFe_{0.8}Ni_{0.2}O_3$: A multiferroic material for low-power spintronic devices with high storage capacity. *ACS Appl. Mater. Interfaces* **2019**, *11*, 31562–31572.

2. Li, L.; Zhou, C.; Zheng, Y.; Du, Y.; Yuan, C.; L.; Ma, L.; Zhao, J.; Rao, G. Thickness-dependent ferromagnetic, ferroelectric, and energy storage perfomances of $(Bi_{0.5}Na_{0.5})_{0.94}Ba_{0.06}TiO_3/La_{0.67}Sr_{0.33}MnO_3$ composite films by pulsed laser deposition. *J. Mater. Sci.: Mater. Electron.* **2023**, *34*, 384.

3. Han, D.-C.; Gong, Z.-X.; Song, N.; Tan, Y.-H.; Li, Y.-K.; Tang, Y.-Z.; Dua, P.-K.; Zhang, H. Ferroelectric properties, narrow band gap and ultra-large reversible entropy change in a novel nonlinear ionic chromium(vi) compound. *Chem. Commun.* **2021**, *57*, 11225–11228.

4. Begué, A.; Ciria, M. Strain-mediated giant magnetoelectric coupling in a crystalline multiferroic heterostructure. ACS *Appl. Mater. Interfaces* **2021**, *13*, 6778–6784.

5. Israel, C.; Mathur, N. D.; Scott, J. F. A one-cent room-temperature magnetoelectric sensor. *Nat. Mater.* **2008**, *7*, 93–94.

6. Wang, Y.; Gray, D.; Berry, D.; Gao, J.; Li, M.; Li, J.; Viehland, D. An extremely low equivalent magnetic noise magnetoelectric sensor. *Adv. Mater.* **2011**, *23*, 4111–4114.

7. Tahir, R.; Fatima, S.; Zahra, S. A.; Akinwande, D.; Li, H.; Hassan, S.; Jafri, M.; Rizwan, S. Multiferroic and ferroelectric phases revealed in 2D Ti_3C2T_xMXene film for high performance resistive data storage devices. *npj 2D Mater. Appl.* **2023**, *7,* 7.

8. Gajek, M.; Bibes, M.; Fusil, S.; Bouzehouane, K.; Fontcuberta, J.; Barthélémy, A.; Fert, A. Tunnel junctions with multiferroic barriers. *Nat. Mater.* **2007**, *6*, 296–302.

9. Garcia, V.; Bibes, M.; Bocher, L.; Valencia, S.; Kronast, F.; Crassous, A.; Moya, X.; Enouz-Vedrenne, S:; Gloter, A.; Imhoff, D.; Deranlot, C.; Mathur, N.D., Fusil, S.; Bouzehouane, K.; Barthélémy, A. Ferroelectric control of spin polarization. *Science* **2010**, *327*, (5969):1106–10.

10. Wang, Y.; Hu, J.; Lin, Y.; Nan, C. W. Multiferroic magnetoelectric composite nanostructures. *NPG Asia Mater.* **2010**, *2*, 61–68.

11. Burns, S. R.; Paull, O.; Juraszek, J:, Nagarajan, V.; Sando, D. The experimentalist's guide to the cycloid, or noncollinear antiferromagnetism in epitaxial $BiFeO_3$. *Adv Mater.* **2020**, 32(45):e2003711.

12. Djani, H.; Garcia-Castro, A.C.; Tong, W.Y.; Barone, P.; Bousquet, E.; Picozzi, S.; Ghosez, P. Rationalizing and engineering Rashba spin-splitting in ferroelectric oxides. *npj Quantum Mater.* **2019**, *4*, 51.

13. Wang, F.; Gao, H.; de Graaf, C.; Poblet, J. M.; Campbell, B. J.; Stroppa, A. Switchable Rashba anisotropy in layered hybrid organic–inorganic perovskite by hybrid improper ferroelectricity. *npj Comput. Mater.* **2020**, *6*, 183.

14. Trier, F.; Noël, P.; Kim, J. V.; Attané, J.-P.; Vila, L.; Bibes, M. Oxide spin-orbitronics: spin–charge interconversion and topological spin textures. *Nat Rev Mater* **2022**, *7*, 258–274.

15. Stroppa, A.; Barone. P; Jain. P; Perez-Mato, J.M.; Picozzi. S. Hybrid improper ferroelectricity in a multiferroic and magnetoelectric metal-organic framework. *Adv Mater.* **2013,** *25*, 2284–2290.

16. Ma, Y.; Sun, Y. Multiferroic and thermal expansion properties of metal-organic frameworks. *J. Appl. Phys.* **2020**, *127*, 080901.

17. Liu, X.-L.; Li, D.; Zhao, H.-X.; Dong, X.-W.; Long, L.-S.; Zheng, L.-S. Inorganic–organic hybrid molecular materials: from multiferroic to magnetoelectric. *Adv. Mater.* **2021**, *33*, 2004542.

18. Zhang, T.; Xu, K.; Li, J.; He, L.; Fu, D.-W.; Ye, Q.; Xiong, R.-G. Ferroelectric hybrid organic–inorganic perovskites and their structural and functional diversity. *Natl. Sci. Rev.* **2022**, *10*, nwac240.

19. Xu. Y.; Luo, Y.; Wu, H.; Meng, Q. Inorganic-organic halide perovskites for new photovoltaic technology. *Natl. Sci. Rev.* **2018,** *5*, 559–576.

20. You, Y.-M.; Liao, W.-Q.; Zhao, D.; Ye, H.-Y.; Zhang, Y.; Zhou, Q.; Niu, X.; Wang, J.; Li, P.-F.; Fu, D.-W.;Wang, Z.; Gao, S.; Yang, K.; Liu, J.-M.; Li, J.; Yan, Y.; Xiong, R.-G. An organic-inorganic perovskite ferroelectric with large piezoelectric response. *Science* **2017**, *357*, 6348.

21. Saparov, B.; Mitzi, D. B. Organic–inorganic perovskites: Structural versatility for functional materials design. *Chem. Rev.* **2016**, *116*, 4558–4596.

22. Xiao, Z.; Yuan, Y.; Shao, Y.; Wang, Q.; Dong, Q.; Bi, C.; Sharma, P.; Gruverman, A.; Huang, J. Giant switchable photovoltaic effect in organometal trihalide perovskite devices. *Nat. Mater.* **2015**, *14*, 193–198.

23. Cai, H.-L.; Zhang, Y.; Fu, D.-W.; Zhang, W.; Liu, T.; Yoshikawa, H.; Awaga, K.; Xiong, R.-G. Above-room-temperature magnetodielectric coupling in a possible molecule-based multiferroic: triethylmethylammonium tetrabromoferrate(III). *J. Am. Chem. Soc.* **2012**, *134*, 18487−18490.

24. Zeng, Y.-L.; Ai, Y.; Tang, S.-Y.; Song, X.-J.; Chen, X.-G.; Tang, Y.-Y.; Zhang, Z.-X.; You, Y.-M.; Xiong, R.-G.; Zhang, H.-Y. Axial-chiral BINOL multiferroic crystals with coexistence of ferroelectricity and ferroelasticity, *J. Am. Chem. Soc.* **2022**, *144*, 19559–19566.

25. Yang, Y.; Ji, J.; Feng, J.; Chen, S.; Bellaiche, L.; Xiang, H. Two-dimensional organic–inorganic room-temprature multiferroics. *J. Am. Chem. Soc.* **2022**, *144*, 14907–14914.

26. He, L.; Shi, P.-P.; Zhou, L.; Liu, Z.-B.; Zhang, W.; Ye, Q. Coexisting ferroelectric and ferroelastic orders in rare 3D homochiral hybrid bimetal halides. *Chem. Mater.* **2021**, *33*, 6233–6239.

27. Burazer, S.; Popović, J.; Jagličić, Z.; Jagodič, M.; Šantić, A.; Altomare, A.; Cuocci, C.; Corriero, N.; Vrankić, M. Magnetoelectric coupling springing up in molecular ferroelectric: [N(C$_2$H$_5$)$_3$CH$_3$][FeCl$_4$]. *Inorg. Chem.* **2020**, *59*, 6876–6883.

28. Fang, Y.-H.; Liu, Z.; Zhou, S.; Fu, P.-X.; Wang, Y.-X.; Wang, Z.-Y.; Wang, Z.-M.; Gao, S.; Jiang, S.-D. Spin-electric coupling with anisotropy-induced vanishment and enhancement in molecular ferroelectrics. *J. Am. Chem. Soc.* **2022**, *144*, 8605–8612.

29. Zhang, H.-Y.; Hu, C.-L.; Hu, Z.-B.; Mao, J.-G.; Song, Y.; Xiong, R.-G. Narrow band gap observed in a molecular ferroelastic: ferrocenium tetrachloroferrate. *J. Am. Chem. Soc.* **2020**, *142*, 3240–3245.

30. Ehrenreich, M. G.; Zeng, Z.; Burger, S.; Warren, M.; Gaultois, M. W.; Tan, J.-C.; Kieslich, G. Mechanical properties of the ferroelectric metal-free perovskite [MDABCO](NH_4)I_3. *Chem. Commun.* **2019**, *55*, 3911–3914.

31. Bermúdez-García, J. M.; Sánchez-Andújar, M.; Castro-García, S.; López-Beceiro, J.; Artiaga, R.; Señarís-Rodríguez, M. A. Giant barocaloric effect in the ferroic organic-inorganic hybrid [TPrA][Mn(dca)$_3$] perovskite under easily accessible pressures. *Nat. Commun.* **2017**, *8*, 15715.

32. Zhou, H.; Ding, H.; Yu, Z.; Yu, T:, Zhai, K.; Wang, B.; Mu, C.; Wen, F.; Xiang, J.; Xue, T.; Wang, L.; Liu, Z.; Sun, Y.; Tian, Y. Pressure control of the structure and multiferroicity in a hydrogen-bonded metal–organic framework. *Inorg. Chem.* **2022**, *61*, 9631–9637.

33. Zhang, Z.-X.; Zhang, H.-Y.; Zhang, W.; Chen, X.-G.; Wang, H.; Xiong, R.-G. Organometallic-based hybrid perovskite piezoelectrics with a narrow band gap. *J. Am. Chem. Soc.* **2020**, *142*, 17787–17794.

34. Hua, X.-N.; Liao, W.-Q.; Tang, Y.-Y.; Li, P.-F.; Shi, P.-P.; Zhao, D.; Xiong, R.-G. A Room Temperature Hybrid lead iodide perovskite ferroelectric. *J. Am. Chem. Soc.* **2018**, *140*, 12296−12302.

35. Liu, G.; Kong, L.; Yang, W.; Mao, H. K. Pressure engineering of photovoltaic perovskites. *Mater. Today* **2019**, *27*, 91–106.

36. Fu, R.; Zhao, W.; Wang, L.; Ma, Z.; Xiao, G.; Zou, B. Pressure-induced emission toward harvesting Cold White light from warm white light. *Angew. Chem. Int. Ed.* **2021**, *60*, 10082–10088.

37. Lü, X.; Yang, W.; Jia, Q.; Xu, H. Pressure-induced dramatic changes in organic–inorganic halide perovskites. *Chem. Sci.* **2017**, *8*, 6764 – 6776.

38. Wang, Y.; Lü, X.; Yang, W.; Wen, T.; Yang, L.; Ren, X.; Wang, L.; Lin, Z.; Zhao, Y. Pressure-induced phase transformation, reversible amorphization, and anomalous visible light response in organolead bromide perovskite. *J. Am. Chem. Soc.* **2015**, *137*, 11144−11149.

39. Jaffe, A.; Lin, Y.; Beavers, C. M.; Voss, J.; Mao, W. L.; Karunadasa, H. I. High-pressure single-crystal structures of 3D lead-halide hybrid perovskites and pressure effects on their electronic and optical properties. *ACS Cent. Sci.* **2016**, *2*, 201–209.

40. Jiang, S.; Fang, Y.; Li, R.; Xiao, H.; Crowley, J.; Wang, C.; White, T. J.; Goddard, W. A., Wang, Z.; Baikie, T.; Fang, J. Pressure-Dependent Polymorphism and Band-Gap Tuning of Methylammonium Lead Iodide Perovskite. *Angew. Chem. Int. Ed.* **2016**, *55*, 6540–6544.

41. Lü, X.; Wang, Y.; Stoumpos, C. C.; Hu, Q.; Guo, X.; Chen, H.; Yang, L.; Smith, J. S.; Yang, W.; Zhao, Y.; Xu, H.; Kanatzidis, M. G.; Jia, Q. Enhanced Structural Stability and Photo Responsiveness of $CH_3NH_3SnI_3$ perovskite via pressure-induced amorphization and recrystallization. *Adv. Mater.* **2016,** *28*, 8663−8668.

42. Altomare, A.; Cuocci, C.; Giacovazzo, C.; Moliterni, A.; Rizzi, R.; Corriero, N.; Falcicchio, A. *EXPO2013*: A Kit of Tools for Phasing Crystal Structures from Powder Data. *J. Appl. Cryst.* **2013**, *46*, 1231–1235.

43. Shi, P.-P.; Tang, Y.-Y.; Li, P.-F.; Liao, W.-Q.; Wang, Z.-X.; Ye, Q.; Xiong, R.-G. Symmetry breaking in molecular ferroelectrics, *Chem. Soc. Rev.* **2016**, *45*, 3811–3827.

44. Xu, G.-C.; Ma, X.-M.; Zhang, L.; Wang, Z.-M.; Gao, S. Disorder−order ferroelectric transition in the metal formate framework of $[NH_4][Zn (HCOO)_3]$. *J. Am. Chem. Soc.* **2010**, *132*, 9588–9590.

45. He, L.; Liu, Y.; Shi, P.; Cai, H.; Fu, D.; Ye, Q. Energy harvesting and Pd(II) sorption based on organic−inorganic hybrid perovskites. *ACS Appl. Mater. Interfaces* **2020**, *12*, 53799–53806.

46. Huang, Y.; Yang, J.; Li, Z.; Qian, K.; Sao, F. High-temperature ferroelastic phase transition in a perovskite-like complex: $[Et_4N]_2[PbBr_3]_2$. *RSC Adv.* **2019**, *9*, 10364.

47. Zheng, X.; Zhou, L.; Shi, P. P.; Geng, F. J.; Fu, D. W.; Ye, Q.; $[(CH_3)_3PCH_2OH][CdBr_3]$ is a perovskite-type ferroelastic compound above room temperature. *Chem. Commun.* **2017**, *53*, 7756−7759.

48. Yin, T.; Yan, H.; Abdelwahab, I.; Lekina, Y.; Lü, X.; Yang, W.; Sun, H.; Leng, K.; Cai, Y.; Shen, Z. X.; Loh, K. P. Pressure driven rotational isomerism in 2D hybrid perovskites. *Nat Commun.* **2023**, *14*, 411.

49. Tokura, Y. Multiferroics—toward strong coupling between magnetization and polarization in a solid. *J. Magn. Magn. Mater.* **2007***, 310, 1145−1150.

50. Ji, L.-J. Ji; Sun, S.-J.; Qin, Y.; Li, K.; Li, W. Mechanical properties of hybrid organic-inorganic perovskites. *Coord. Chem. Rev.* **2019**, *391*, 15−29.

51. Gan, L.; Romero, F. J.; Franco, V.; Martin-Olalla, J.-M.; Gallardo, M. C.; Salje, E. K. H.; Zhou, Y.; Aktas, O. Correlations between elastic, calorimetric, and polar properties of ferroelectric $PbSc_{0.5}Ta_{0.5}O_3$ (PST). *Appl. Phys. Lett.* **2019**, *115*, 161904.

52. Yang, D.: Wang, W.; Yang, T.; Lampronti, G. I.; Ye, H.; Wu, L.; Yu, Q.; Lu, S. Role of spontaneous strains on the biphasic nature of partial B-site disorder double perovskite La_2NiMnO_6. *APL Mater.* **2018,** *6*, 066102.

53. Wang, Z.-X.; Zhang, H.; Wang, F.; Cheng, H.; He, W.-H. ; Liu, Y.-H.; Huang, X.-Q.; Li, P.-F. Superior transverse piezoelectricity in a halide perovskite molecular ferroelectric thin film. *J. Am. Chem. Soc.* **2020**, *142*, 12857.

54. Zeng, Y. L.; Ai, Y.; Tang, S. Y.; Song, X. J.; Chen, X. G.; Tang, Y. Y.; Zhang, Y. X.; You, Y. M.; Xiong, R. G.; Zhang H. Y. Axial-Chiral BINOL multiferroic crystals with coexistence of ferroelectricity and ferroelasticity. *J. Am. Chem. Soc.* **2022**, *144*, 19559–19566.

55. Altomare, A.; Campi, G.; Cuocci, C., Eriksson, L., Giacovazzo, C., Moliterni, A.; Rizzi, R., Werner, P.-E. Advances in Powder Diffraction Pattern Indexing: *N-TREOR09*. *J. Appl.Cryst.* **2009**, *42*, 768–775.

56. Boultif, A. & Louer, D. Powder pattern indexing with the dichotomy method. *J. Appl. Cryst.* **2004**, *37*, 724-731.

57. Szafrański, M. Large negative linear compressibility triggered by hydrogen bonding. *J. Phys. Chem. C*, **2020**, *124*, 11631–11638.

58. Fang, Y.; Zhang, L.; Yu, Y.; Yang, X.; Wang, K.; Zou, B. Manipulating Emission enhancementand piezochromism in two-dimensional organic–inorganic halide perovskite $[(HO)(CH_2)_2NH_3)]_2PbI_4$ by high pressure. *CCS Chem.* **2020**, *2*, 2203–2210.

59. Jaffe, A., Lin, Y.; Karunadasa, H. I. Halide perovskites under pressure: accessing new properties through lattice compression. *ACS Energy Lett*. **2017**, *2*, 1549–1555.

60. Sahoo, S.; Ravindran, T. R.; Srihari, V.; Pandey, K. K.; Chandra, S.; Thirmal, C.; Murugavel, P. Pressure induced phase transformations in diisopropylammonium bromide. *J. Solid State Chem*. **2019**, *274*, 182–187.

61. Lee, Y.; Mitzi, D. B.; Barnes, P. W.; Vogt, T. Pressure-induced phase transitions and templating effect in three-dimensional organic-inorganic hybrid perovskites. *Phys. Rew B* **2003**, *68*, 020103.

62. Li, Q.; Yin, L.; Chen, Z.; Deng, K.; Luo, S.; Zou, B.; Wang, Z.; Tang, J.; Quan, Z. High pressure structural and optical properties of two-dimensional hybrid halide perovskite $(CH_3NH_3)_3Bi_2Br_9$. *Inorg. Chem.* **2019**, *58*, 1621–1626.

63. Sun, S.; Fang, Y.; Kieslich, G.; White, T. J.; Cheetham, A. K. Mechanical properties of organic–inorganic halide perovskites, $CH_3NH_3PbX_3$ (X = I, Br and Cl), by nanoindentation. *J. Mater. Chem. A*, **2015**, *3*, 18450–18455.

64. Sun, S.; Isikgor, F. H.; Deng, Z.; Wei, F.; Kieslich, G.; Bristowe, P. D.; Ouyang, J.; Cheetham, A. K. Factors influencing the mechanical properties of formamidinium lead halides and related hybrid perovskites. *ChemSusChem* **2017**, *10,* 3740–3745.

65. Fischer, G. J.; Wang, Z.; Karato, S. I. Elasticity of $CaTiO_3$, $SrTiO_3$ and $BaTiO_3$ perovskites up to 3.0 GPa: the effect of crystallographic structure. *Phys. Chem. Miner.* **1993**, *20*, 97–103.

66. Hu, Y.; Parida, K.; Zhang, H.; Wang, X.; Li, Y.; Zhou, X.; Morris, S. Al.; Liew, W. H.; Wang, H.; Li, T.; Jiang, F.; Yang, M.; Alexe, M.; Du, Z.; Gan, C. L.; Yao, K.; Xu, B.; Lee, P. S.; Fan, H. J. Bond engineering of molecular ferroelectrics renders soft and high performance piezoelectric energy harvesting materials. *Nat. Commun.* **2022**, 13:5607.

67. Clark, R. J. H.; Dunn, T. M. The infrared spectra of some tetrahedral inorganic complex halides. *J. Chem. Soc.* **1963**, 1198–1201.

68. Avery, J. S.; Burbridge, C. D.; Goodgame, D. M. L. Raman spectra of tetrahalo-anions of Fe^{III}, Mn^{II}, Fe^{II}, Cu^{II} and Zn^{I} Spectrochim. *Acta Part A: Mol. Spectros.* **1968**, *24*, 1721–1726.

69. Boldyreva, E. V. High-pressure diffraction studies of molecular organic solids. A personal view. *Acta Crystallogr. Sect. A Found. Crystallogr.* **2008**, *64*, 218–231.

70. Clune, A.; Harms, N.; O'Neal, K. R.; Hughey, K.; Smith, K. A.; Obeysekera, D.; Haddock, J.; Dalal, N. S.; Yang, J.; Liu, Z.; Musfeldt, J. L. Developing the pressure−temperature−magnetic

field phase diagram of multiferroic [(CH$_3$)$_2$NH$_2$]Mn(HCOO)$_3$. *Inorg. Chem.* **2020**, *59*, 10083−10090.

71. Jaffe, A.; Lin, Y.; Mao, W. L.; Karunadasa, H. I. Pressure-induced conductivity and zellow-to-black piezochromism in a layered Cu-Cl hybrid perovskite. *J. Am. Chem. Soc.* **2015**, *137*, 1673−1678.

72. Wang, S.; Liu, X.; Li, L.; Ji, C.; Sun, Z.; Wu, Z.; Hong, M.; Luo, J. An unprecedented biaxial trilayered hybrid perovskite ferroelectric with directionally tunable photovoltaic effects. *J. Am. Chem. Soc.* **2019**, *141*, 7693−7697.

73. Chen, X.-G.; Song, X.-J.; Zhang, Z.-X.; Li, P.-F.; Ge, J.-Z.; Tang, Y.-Y.; Gao, J.-X.; Zhang, W.-Y.; Fu, D.-W.; You, Y.-M.; Xiong, R.-G. Two-dimensional layered perovskite ferroelectric with giant piezoelectric voltage coefficient. *J. Am. Chem. Soc.* **2020**, *142,* 1077−1082.

74. Ye, H.-Y.; Liao, W.-Q.; Hu, C.-L.; Zhang, Y.; You, Y.-M.; Mao, J.-G.; Li, P.-F.; Xiong, R.-G. Bandgap engineering of lead-halide perovskite-type ferroelectrics. *Adv. Mater. 2016*, **28**, 2579−2586.

75. Chen, H.; Liu, K.; Hu, L.; Al-Ghamdi, A. A.; Fang, X. New concept ultraviolet photodetectors. *Mater. Today* **2015**, *18*, 493−502.

76. Shockley, W.; Queisser, H. J. Detailed balance limit of efficiency of p-n junction solar cells. *J. Appl. Phys.* **1961**, *32*, 510−519.

77. Fang, Y.; Zhang, L.; Wu, L.; Yan, J.; Lin, Y.; Wang, K.; Mao, W. L.; Zou, B. Pressure-induced emission (PIE) and phase transition of a two-dimensional halide double perovskite (BA)$_4$AgBiBr$_8$ (BA = CH$_3$(CH$_2$)$_3$NH$_3$$^+$). *Angew. Chem. Int. Ed.* **2019**, *58*, 15249−15253.

78. Liu, G.; Gong, J.; Kong, L.; Schaller, R. D.; Hu, Q.; Liu, Z.; Yan, S.; Yang, W.; Stoumpos, C. C.; Kanatzidis, M. G.; Mao, H.-K.; Xu, T. Isothermal pressure-derived metastable states in 2D

hybrid perovskites showing enduring bandgap narrowing. *Proc. Natl. Acad. Sci. U.S.A.* **2018**, *115*, 8076−8081.

79. Shi, Y.; Ma, Z.; Zhao, D.; Chen, Y.; Cao, Y.; Wang, K.; Xiao, G.; Zou, B. Pressure-induced emission (PIE) of one-dimensional organic tin bromide perovskites. *J. Am. Chem. Soc.* **2019**, *141*, 6504–6508.

80. Ma, Z.; Liu, Z.; Lu, S.; Wang, L.; Feng, X.; Yang, D.; Wang, K.; Xiao, G.; Zhang, L.; Redfern, S. A. T.; Zou, B. Pressure- induced emission of cesium lead halide perovskite nanocrystals. *Nat. Commun.* **2018**, *9*, 4506.

81. Ma, Z.; Li, F.; Sui, L.; Shi, Y.; Fu, R.; Yuan, K.; Xiao, G.; Zou, B. Tunable Color Temperatures and Emission Enhancement in 1D Halide Perovskites under High Pressure. *Adv. Opt. Mater*. **2020**, *8*, 2000713.

82. Shi, Y.; Zhao, W.; Ma, Z.; Xiao, G.; Zou, B. Self-trapped exciton emission and piezochromism in conventional 3D lead bromide perovskite nanocrystals under high pressure. *Chem. Sci.* **2021**, *12*, 14711–14717.

83. Kang, L.; Lin, Z. Regulation strategy of white emission from organic–inorganic hybrid metal halide perovskites. *Inorg. Chem. Front.* **2023**, *10*, 13–36.

84. Lü, X.; Hu, Q.; Yang, W.; Bai, L.; Sheng, H.; Wang, L.; Huang, F.; Wen, J.; Miller, D. J.; Zhao, Y. *J. Am. Chem. Soc.* **2013**, *135*, 13947.

85. Ma, Y.; Eremets, M.; Oganov, A. R.; Xie, Y.; Trojan, I.; Medvedev, S.; Lyakhov, A.O.; Valle, M.; Prakapenka, V. *Nature* **2009**, *458*, 182.

86. Zhang, L.; Liu, C.; Wang, L.; Liu, C.; Wang, K.; Zou, B. Pressure-Induced Emission Enhancement, Band Gap Narrowing and Metallization of Halide Perovskite $Cs_3Bi_2I_9$. *Angew. Chem. Int. Ed.* **2018**, *57*, 11213–11217.

For Table of Contents Only